Chemical potential and symmetry energy for intermediate-mass fragment production in heavy ion reactions near the Fermi energy

X. Liu,[1] W. Lin,[1,*] M. Huang,[2] R. Wada,[3,†] J. Wang,[1] A. Bonasera,[3,4] H. Zheng,[4] Z. Chen,[1] S. Kowalski,[5] T. Keutgen,[6] K. Hagel,[3] L. Qin,[3] J. B. Natowitz,[3] T. Materna,[3] P. K. Sahu,[3] M. Barbui,[3] C. Bottosso,[3] and M. R. D. Rodrigues[3]

[1]*Institute of Modern Physics, Chinese Academy of Sciences, Lanzhou 730000, China*

[2]*College of Physics and Electronics Information, Inner Mongolia University for Nationalities, Tongliao 028000, China*

[3]*Cyclotron Institute, Texas A&M University, College Station, Texas 77843, USA*

[4]*Laboratori Nazionali del Sud, INFN, via Santa Sofia, 62, 95123 Catania, Italy*

[5]*Institute of Physics, Silesia University, Katowice, Poland*

[6]*FNRS and IPN, Université Catholique de Louvain, B-1348 Louvain-Neuve, Belgium*

(Received 15 September 2015; revised manuscript received 29 January 2017; published 4 April 2017)

Ratios of differential chemical potential values relative to the temperature, $(\mu_n - \mu_p)/T$, extracted from isotope yields of 13 reaction systems at 40 MeV/nucleon are compared to those of a quantum statistical model to determine the temperature and symmetry energy values of the fragmenting system. The experimental $(\mu_n - \mu_p)/T$ values are extracted based on the modified Fisher model. Using the density value of $\rho/\rho_0 = 0.56$ from the previous analysis, the temperature and symmetry energy values of $T = 4.6 \pm 0.4$ MeV and $a_{\rm sym} = 23.6 \pm 2.1$ MeV are extracted in a framework of a quantum statistical model. These values agree well with those of the previous work, in which a self-consistent method was utilized with antisymmetrized molecular dynamics simulations. The extracted temperature and symmetry energies are discussed together with other experimental values published in literature.

DOI: 10.1103/PhysRevC.95.044601

I. INTRODUCTION

The symmetry energy of nuclear matter is a fundamental ingredient in the investigation of nuclear and astrophysical phenomena [1,2]. In violent collisions of heavy ion reactions near the Fermi energy, different sizes of clusters, from deuterons to intermediate mass fragments (IMFs) with $3 \leqslant Z < 20$, are copiously produced. The experimentally observed multiplicity distribution of isotopes for a given Z shows a quasi-Gaussian shape with a peak near $N = Z$ as a function of mass [3]. This suggests that the production of these isotopes is closely related to the symmetry energy, since the symmetry energy term is in proportional to $(N - Z)^2$ in the Weizsäcker-Bethe semiclassical mass formula [4,5]. However the production mechanism of these clusters is still debated. Global characteristic features of the experimental observables, such as multiplicity, mass or charge distributions and energy spectra, are investigated both by statistical multifragmentation models [6,7] and by transport models [8–15], although they are based on quite different assumptions. The former employs a freezeout concept, under which the multifragmentation process takes place in equilibrated nuclear matter described by parameters such as size, neutron/proton ratio, density and temperature. Piantelli *et al.* analyzed the multifragmentation events of ^{129}Xe $+^{\rm nat}$ Sn at 30 to 50 MeV/nucleon, based on a statistical model, i.e., a microcanonical multifragmentation model (MMM) [16]. By optimizing parameters, they could reproduce the experimental results very well. Fragment excitation energies of 3.0 to 3.5 MeV/nucleon and an emission volume of 3.9 to 5.7 V_0, where V_0 is the volume of the composite system at normal density, were extracted as the freezeout properties of the multifragmenting system. On the other hand, Zbiri *et al.* analyzed the events from Au +Au at 60 and 150 MeV/nucleon using a quantum molecular dynamics transport model (QMD) [17], in which nucleon propagation in a mean field and nucleon-nucleon collisions under Pauli blocking are two main physical ingredients. They also reproduced the global features of the experimental results and concluded that the dynamical processes play a significant role in the multifragmentation. In our previous works, similar results were also obtained in reactions, ^{64}Zn + ^{58}Ni, ^{92}Mo, ^{197}Au between 35 to 79 MeV/nucleon, where the antisymmetrized molecular dynamics (AMD) code of Ono *et al.* [14,18–21] was employed [22,23]. In our recent work of Ref. [24], we suggested that a freezeout occurs in AMD simulations. This conclusion was reached by studying the density and temperature of the fragmenting source as a function of the incident energy, utilizing a self-consistent method [25,26] for ^{40}Ca + ^{40}Ca at 35 to 300 MeV/nucleon. This result provides a bridge between the statistical multifragmentation models and the transport models.

Investigations of the symmetry energy, especially focussing on its density dependence, have been conducted using many observables such as isotopic ratios [27], isospin diffusion [28], neutron-proton emission ratios [29], giant monopole resonances [30], pygmy dipole resonances [31], giant dipole resonances [32], collective flow [33], and isoscaling [34–36] among others. Ono *et al.* introduced a generalized free energy, $K(N, Z)$, and extracted the symmetry energy coefficient relative to the temperature, $a_{\rm sym}/T$, from quadratic distributions of the IMF yields [37,38]. In our previous works, $a_{\rm sym}/T$ was experimentally extracted using isobaric yield ratios [39,40] and m-scaling [41] within the framework of the modified

*linwp1204@impcas.ac.cn

†wada@comp.tamu.edu

Fisher model (MFM) [42–45]. In Ref. [25], we proposed a self-consistent method based on MFM to evaluate the density, temperature and symmetry energy by comparing the experimental $a_{\rm sym}/T$ values to those for the primary fragments generated by AMD with three different density-dependent symmetry energy interactions. Applying this method to the experimentally reconstructed primary isotope yields from the reaction of 40 MeV/nucleon ^{64}Zn + ^{112}Sn system [3], we extracted $\rho/\rho_0 = 0.56 \pm 0.02$, $T = 5.2 \pm 0.6$ MeV, and $a_{\rm sym} = 20.8 \pm 0.6$ MeV for the fragmenting system [26].

In this work, the ratio of proton-neutron differential chemical potential relative to the temperature, $(\mu_n - \mu_p)/T$ (hereafter denoted as $\Delta\mu/T$), is extracted from the isotope yields from 13 reaction systems. These results are compared to those predicted by the quantum statistical model (QSM) of Harn and Stöcker [46] to determine the temperature and symmetry energy of the fragmenting systems. This article is organized as follows. In Sec. II, we briefly summarize the experiment. In Sec. III, the moving-source fit, the extraction of the temperatures, and symmetry energies of the fragmenting systems are described and the results are presented. In Sec. IV, symmetry energy extraction at Fermi energies and symmetry energy constraints at subsaturation densities are discussed. In Sec. V, a summary is given.

II. EXPERIMENT

The experiment was performed at the K-500 superconducting cyclotron facility at Texas A&M University. ^{64,70}Zn and ^{64}Ni beams were used to irradiate ^{58,64}Ni, ^{112,124}Sn, ^{197}Au, and ^{232}Th targets at 40 MeV/nucleon. 13 reaction systems were analyzed for the present work. They are ^{64}Zn + ^{112}Sn, ^{70}Zn, ^{64}Ni on ^{112,124}Sn, ^{58,64}Ni, ^{197}Au, ^{232}Th. Intermediate mass fragments (IMFs) were detected by a detector telescope placed at 20°. The telescope consisted of four Si detectors. Each Si detector was 5 cm × 5 cm. The nominal thicknesses were 129, 300, 1000, 1000 μm, respectively. All four Si detectors were segmented into four sections and each quadrant had a 5° opening in polar angle. Typically 6 ∼ 8 isotopes for atomic numbers Z up to $Z = 18$ were clearly identified with the energy threshold of 4 ∼ 10 MeV/nucleon, using the $\Delta E - E$ technique for any two consecutive detectors. Mass identification of the isotopes was made using a range-energy table [47]. The yields of light charged particles (LCPs) in coincidence with IMFs were also measured using 16 single-crystal CsI(Tl) detectors of 3 cm length set around the target at angles between $\theta_{\rm lab} = 27°$ and $\theta_{\rm lab} = 155°$. The light output from each detector was read by a photomultiplier tube. The pulse shape discrimination method was used to identify p, d, t, ^{3}He, and α particles. The energy calibrations for these particles were performed using Si detectors (50 ∼ 300 μm) in front of the CsI detectors in separate runs. For the neutron detection, 16 detectors of the Belgian-French neutron detector array DEMON (Detecteur Modulaire de Neutrons) [48] were used. The detectors were distributed to achieve opening angles between the telescope and the detector of $15° \leqslant \theta_{{\rm IMF}-n} \leqslant 160°$. Neutron/$\gamma$ discrimination was obtained from a pulse shape analysis, by comparing the slow component of the light output to the total light output. The neutron detection efficiency of the DEMON detector, averaged over the whole volume, was calculated using the GEANT code [49].

The event class identification in this experiment is crucial for the following analysis. The events triggered by IMFs in this experiment are "inclusive", but they belong to a certain class of events. In the experiment, the telescope at $\theta = 20°$ was used as the main trigger. The angle of the telescope was optimized to be small enough so that sufficient IMF yields were obtained above the detector energy threshold but large enough so that the contribution from peripheral collisions was negligible. In order to understand the event class taken in this experiment, based on the analysis in Ref. [23], AMD simulations [20] are used to evaluate the impact parameter range in the present data set. According to the comparison between the experiment and AMD simulations, it is found that IMFs are generated copiously in a wide impact parameter range more or less equally, that is, more than 80% of the observed IMF yields originate from the impact parameter range $b \leqslant 8$ fm. A detailed discussion is given in Ref. [50].

In order to further define the properties of fragmenting source involved in the reaction products, a moving-source fit technique is employed, which is described below.

III. RESULTS

A. Moving-source analysis

In order to characterize the fragmenting source, a moving-source analysis is employed. A detail description of a moving-source method is given in Ref. [51] and a partial analysis of the moving-source fit performed for IMFs in this analysis has been given in Refs. [40,50], and therefore, a brief description for neutrons and light-charged particles (LCPs) is presented here. Some of typical energy spectra of neutrons and LCPs in coincidence with IMFs are shown in Fig. 1. No ^{3}He spectra are shown because of poor identification in CsI and/or poor statistics. Since the measured angles are larger than $\theta_{\rm lab} > 20^o$ where the projectile-like fragment (PLF) source component has negligible contributions to these spectra, two sources, a nucleon-nucleon (NN) source and a target-like fragment (TLF) source are used for the moving-source fit. The NN source has a source velocity close to a half-beam velocity and is described by a volume type Maxwellian, and the TLF source has a small source velocity with a surface type Maxwellian [51]. In order to optimize the four parameters in each source, multiplicity, slope parameter, the Coulomb energy for LCPs, and source velocity, Minuit in the Cern library has been used. Typical fit results are shown by different (color) lines as specified in the figure caption. As one can see, two source components, NN and TLF, dominate in distinct two angular ranges, that is, the NN source dominates in the top three to four spectra and the TLF source dominates in the bottom three to four spectra for all cases studied. Therefore four parameter values for each source are essentially determined by the spectra in these two distinct angular ranges. The extracted multiplicity values of the NN source of neutrons, LCPs and IMFs for all 13 reactions are given in Supplemental Material of this article [52]. The errors given are estimated as follows. MINUIT gives errors for each searched parameter. However in most cases resultant errors for the multiplicities are in an order

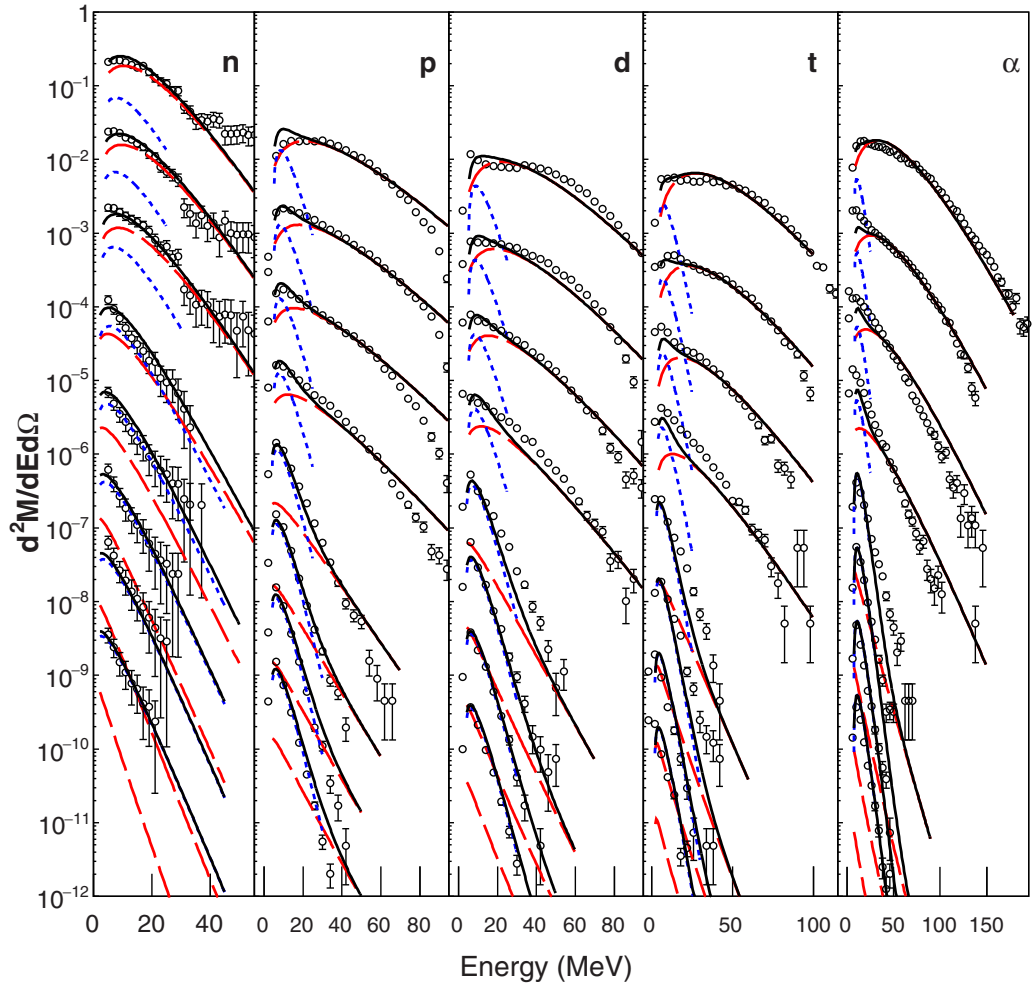

FIG. 1. Neutrons and light charged particle energy spectra at different θ_{lab} in coincidence with IMFs with $Z \geqslant 3$ for the $^{64}Ni + ^{112}Sn$ reaction. The differential multiplicity is given in the absolute scale, but multiplied by a factor of $10^n (n = 0–7)$ from the top to the bottom spectra. For neutrons, $\theta_{lab} = 25°,31°,40°,67°,85°,104°,120°,140°$ and for LCPs, $\theta_{lab} = 36°,47°,57°,70°,115°,135°,145°,155°$ from top to bottom. Red dashed lines represent the NN-source component, blue dotted lines for the TLF source component, and the black solid lines for the summation of them.

of 1% or less, because there are many local minima for the multiple parameter fits. In order to get more realistic errors for the multiplicities, several different optimizations have been performed, which includes different initial values, a fixed source velocity or energy slope with an averaged values, fixed parameter values in different angular ranges. The extracted multiplicities within 10% from the minimum χ-square values are plotted as a function of multiplicity. For LCPs and neutrons, 10% of the multiplicity values are estimated as the maximum differences for different optimization conditions. For neutrons, an additional 5% error is added from the neutron efficiency calculation [49]. These values are set as the errors of the multiplicities, if the error given by MINUIT is smaller. In a few case the errors from the MINUIT is larger than this criterion and the error is taken as in the table. For IMFs, two independent data sets for $^{64}Zn + ^{112}Sn$ are analyzed independently and the difference in multiplicity values are plotted as a function of the multiplicity. The differences distribute around 5% for $M \sim 0.3$ to 50% for $M \leqslant 0.001$. These are generally much larger than the errors given by MINUIT. The differences are fit by a function $f(M)$ to evaluate the maximum for a given M value. Most of the differences are smaller than an empirical function $f(M) = 0.03M^{0.6}$ with an upper limit of 50%. This function is used to estimate the errors for the IMFs multiplicity in the Supplemental Material [52].

B. NN-source size and Z/A ratio

The size and Z/A ratio of the NN source [A_{NN} and $(Z/A)_{NN}$] are directly evaluated using the NN-source multiplicities (M) given in the Supplemental Material [52] as

$$A_{NN} = \sum_i A_i M_i, \tag{1}$$

$$(Z/A)_{NN} = \left(\sum_i Z_i M_i\right) \Big/ \left(\sum_i A_i M_i\right), \tag{2}$$

where A_i and Z_i are the mass and charge numbers of the ith isotope and the summation is taken over all measured particles, including neutrons, LCPs, and IMFs with Z up to 18. We have

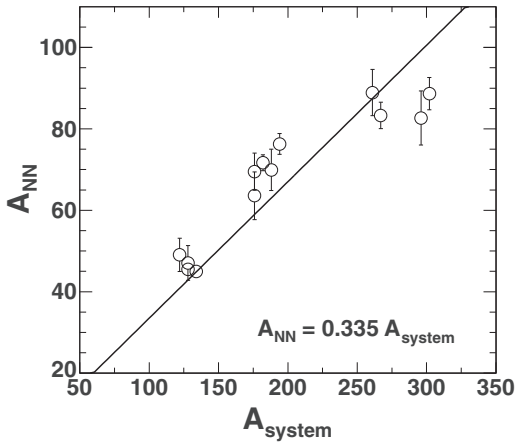

FIG. 2. NN-source size versus system size, where $A_{\rm syst} = A_{\rm proj} + A_{\rm targ}$. Data points are fit by a linear function and the parameters are shown in the figure.

found that the contribution of the $Z > 18$ IMFs, which were not isotropically identified in the experiment and are missing in Eqs. (1) and (2), is less than 1%. In Figs. 2 and 3, the size and Z/A ratio of the NN source are plotted as functions of those of the system, respectively. As shown in Fig. 2, the NN-source size varies from ∼40 to ∼90, which is much smaller than the size of each reaction system studied (from 122 to 302). This rather small size of the NN source indicates that the particles are commonly produced by a multifragmentation of a part of the projectile-target overlap region, and this similarity of the production mechanism enables us to analyze the data from quite different reaction systems on a common basis as seen in our previous works [38–41]. Figure 3 indicates that the Z/A ratios of the NN sources are distributed slightly below the values of the 1 to 1 mixing of the projectile and the target nucleons (dashed line), that is, the NN source is always slightly more neutron-rich than those of the simple overlap

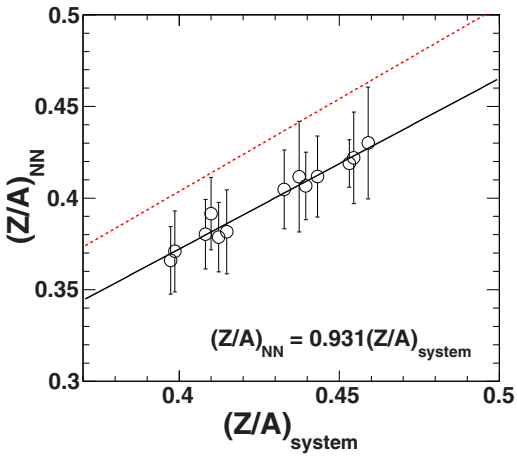

FIG. 3. NN-source Z/A versus system Z/A, where $(Z/A)_{\rm syst} = (Z_{\rm proj} + Z_{\rm targ})/(A_{\rm proj} + A_{\rm targ})$. Data points are fit by a linear function (solid line) and the parameters are shown in the figure. Dashed line indicates the values of 1 to 1 mixing between the projectile and target for all 13 systems.

region of the projectile and target. This is an experimental indication for the neutron migration from the cool projectile-like and target-like zones to the hot overlap zone in the heavy ion collisions at Fermi energies [34,36]. This phenomenon, which is called isospin migration or isospin fractionation, has been also predicted by model simulations of the semiperipheral collisions at this energy region [10,53,54].

As shown in Figs. 2 and 3, both A_{NN} vs $A_{\rm syst}$ and $(Z/A)_{NN}$ vs $(Z/A)_{\rm syst}$ plots show rather linear relations. The obtained results are fit by linear functions, respectively, and the fitting results are given by

$$A_{NN} = 0.335 A_{\rm syst}, \tag{3}$$

$$(Z/A)_{NN} = 0.931 (Z/A)_{\rm syst}. \tag{4}$$

C. Differential chemical potential relative to temperature

The ratio of differential chemical potential relative to the temperature, $\Delta\mu/T$, can be extracted from the isotopic yield ratios, using the MFM [42]. The formulation of MFM is given in the Appendix. In the framework of MFM, thermal and chemical equilibriums are assumed, and the yield of an isotope with mass A and $I = N - Z$ (N neutrons and Z protons) produced in a multifragmentation reaction, can be given as [38–45,55]

$$Y(I,A) = Y_0 A^{-\tau} \exp\left[\frac{W(I,A) + \mu_n N + \mu_p Z}{T} + S_{\rm mix}\right]. \tag{5}$$

$A^{-\tau}$ represents the entropy of the fragment from $T\tau lnA$ in Eq. (A6) in the Appendix and $S_{\rm mix}$ is the mixing entropy defined in Eq. (A12) in the Appendix. As noted in the Errata in Refs. [26,59], the MFM formula in Refs. [43,44] has an error in describing the mixing entropy as an opposite sign. This has been corrected in the present work. τ is the critical exponent. In the present work, the value of $\tau = 2.3$ is adopted from the previous studies [45]. Using the generalized Weizsäcker-Bethe semiclassical mass formula [4,5], $W(I,A)$ can be approximated as

$$\begin{aligned} W(I,A) &= a_v A - a_s A^{2/3} - a_c \frac{Z(Z-1)}{A^{1/3}} \\ &\quad - a_{\rm sym} \frac{(N-Z)^2}{A} - a_p \frac{\delta_p}{A^{1/2}}, \\ \delta_p &= -\frac{(-1)^Z + (-1)^N}{2}. \end{aligned} \tag{6}$$

μ_n (μ_p) is the neutron (proton) chemical potential. In general coefficients (a_v, a_s, a_c, $a_{\rm sym}$, and a_p) and the chemical potentials are temperature and density dependent. In the given formulation in the Appendix, a constant volume process is assumed in the free energy, and therefore the term "symmetry energy" is used throughout this work. If one assumes a constant pressure [56], the term "symmetry enthalpy" should be used. Experimentally, the exact conditions can not be determined, and thus we use "symmetry energy" throughout this article [57]. In Eq. (6), the symmetry term is given as a net symmetry energy of the volume and surface contributions [58]. This is because at a finite temperature, notable surface dependence

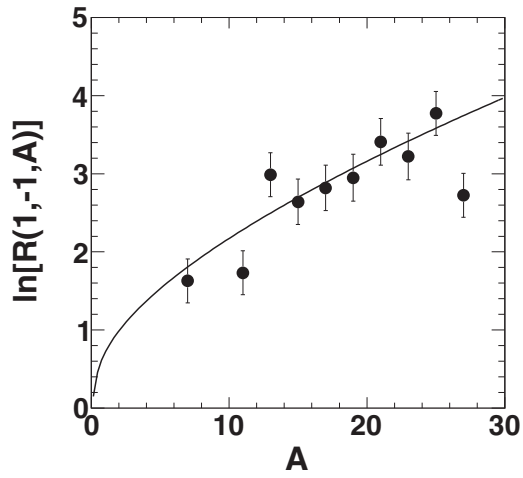

FIG. 4. $\ln[R(1,-1,A)]$ as a function of A directly from the experimentally observed IMF yield from ^{64}Zn + ^{112}Sn. The curve is the fit of data points using Eq. (8). The optimized $\Delta\mu/T$ and a_c/T values are 0.71 and 0.35, respectively.

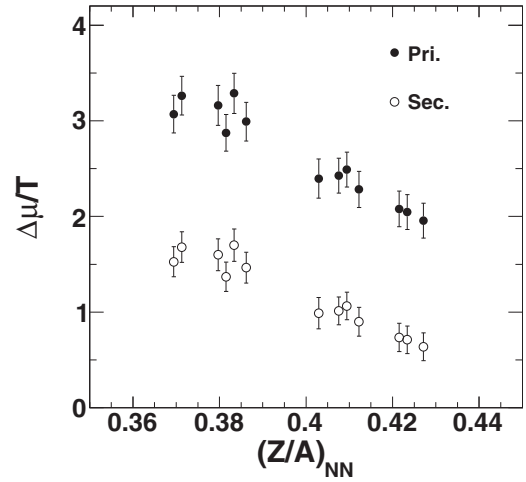

FIG. 5. Open circles: the $\Delta\mu/T$ values from the experimentally observed IMF yields from all 13 systems as a function of $(Z/A)_{NN}$; full circles: the "primary" $\Delta\mu/T$ values feeded using Eq. (9) as a function of $(Z/A)_{NN}$, where $(Z/A)_{NN}$ is calculated using Eq. (2).

of the symmetry energy is not observed in AMD simulations [25,36,39] and experiments [26,38,50].

Following Ref. [39], the isotope yield ratio between isobars with $I+2$ and I, $R(I+2,I,A)$, is utilized, which is

$$\begin{aligned} R(I+2,I,A) &= Y(I+2,A)/Y(I,A) \\ &= \exp\{[\mu_n - \mu_p + 2a_c(Z-1)/A^{1/3} \\ &\quad - 4a_{\rm sym}(I+1)/A - \delta(N+1,Z-1) \\ &\quad - \delta(N,Z)]/T + \Delta(I+2,I,A)\}, \end{aligned} \tag{7}$$

where $\Delta(I+2,I,A) = S_{\rm mix}(I+2,A) - S_{\rm mix}(I,A)$ and $S_{\rm mix}(I,A) = -[N\ln(N/A) + Z\ln(Z/A)]$. When the above equation is applied for a pair of mirror nuclei of odd mass isotopes with $I=-I$ and I, the symmetry energy term, pairing term, and mixing entropy terms drop out and the following equation is obtained:

$$\ln[R(I,-I,A)]/I = [\Delta\mu + a_c(A-1)/A^{1/3}]/T. \tag{8}$$

The left side of Eq. (8) is calculated from the experimentally obtained mirror isobar yields, and $\Delta\mu/T$ and a_c/T are optimized by fitting the calculated $\ln[R(I,-I,A)]/I$ using the right side of Eq. (8). Focusing on the $I=1$ and $I=-1$ isotopes, for a typical system ^{64}Zn + ^{112}Sn, the $\ln[R(1,-1,A)]$ values as a function of A and the corresponding fit using Eq. (8) are given in Fig. 4. Similar quality results are obtained for the other reaction systems [39]. Using the fact that the Coulomb term in Eq. (8) is only related to the chosen isotopes and therefore independent of the different reaction systems under similar fragmenting conditions, the same a_c/T value from the ^{64}Zn + ^{112}Sn reaction is used to extract the $\Delta\mu/T$ values as free parameters from the different reaction systems [39]. The resultant $\Delta\mu/T$ values extracted from all 13 systems are plotted as a function of $(Z/A)_{NN}$ using open symbols in Fig. 5, where $(Z/A)_{NN}$ is calculated using Eq. (2). A monotonically decreasing trend of the experimental (secondary) $\Delta\mu/T$ as $(Z/A)_{NN}$ increases is observed in Fig. 5. This trend is a natural consequence of the decreasing neutron richness of the extracted source.

D. Sequential feeding for $\Delta\mu/T$

When fragments are emitted from the source, many of them are in excited states and cool by evaporation processes before they are detected. The sequential decay of these primary hot fragments significantly alters the yield distribution and distorts the information in the primary yields [50,59,60]. The sequential decay process is employed in slightly different ways in three models used in this analysis, AMD+GEMINI [61], SMM, and QSM, but the sequential decay process is well established and well coded. Therefore, for a quantitative evaluation of the sequential decay effect on $\Delta\mu/T$, the statistical multifragmentation model (SMM) of Bondorf *et al.* [7,62] is employed. SMM assumes fragments are formed in a given source under a statistical equilibrium within a freezeout volume. In the thermodynamic limit, this process in SMM is consistent with a possible nuclear liquid-gas phase transition [63–65]. These hot primary fragments propagate independently in their mutual Coulomb field and undergo de-excitation to the ground state. The calculated yields of the cold fragments after the secondary decays reasonably reproduce the experimental data from both peripheral and central heavy ion collisions at intermediate energies [66–68].

For the present analysis, SMM is utilized to simulate the breakup of $A=100$ sources with different Z numbers (i.e., $Z=45$, 50, and 55), under different excitation energies (i.e., $E_x=5$ and 10 MeV), different freezeout volumes (i.e., $V/V_0=3.0$, 5.0, and 10.0). For each case, 1×10^5 events are computed, and both primary and secondary production yields are determined. Following the same method mentioned in Sec. III(b), $\Delta\mu/T$ values are extracted from the primary and secondary isotope yields generated by SMM. The relations between the extracted primary and secondary $\Delta\mu/T$ [$(\Delta\mu/T)_{Pri}$ and $(\Delta\mu/T)_{Sec}$] values are shown in Fig. 6, for the

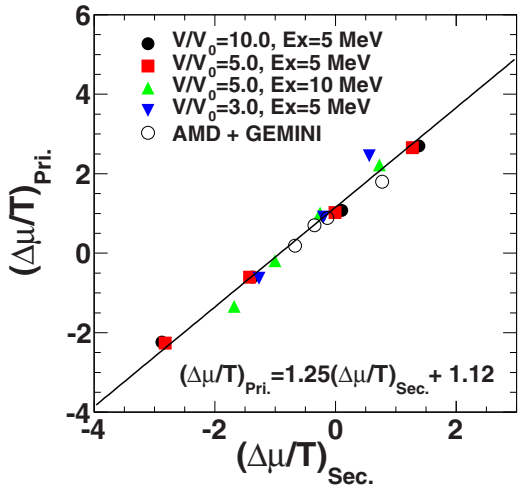

FIG. 6. Calculated $(\Delta\mu/T)_{Pri}$ vs $(\Delta\mu/T)_{Sec}$. The results from the SMM calculations are shown by solid symbols and those from the AMD-GEMINI are shown by open circles. The reaction systems used for the AMD+GEMINI simulation are ^{58}Ni + ^{58}Ni, ^{58}Fe + ^{58}Fe at 45 MeV/nucleon and ^{64}Zn + ^{112}Sn and ^{64}Ni + ^{124}Sn at 40 MeV/nucleon. Data points from SMM are globally fit by a linear function and the parameters are shown in the figure.

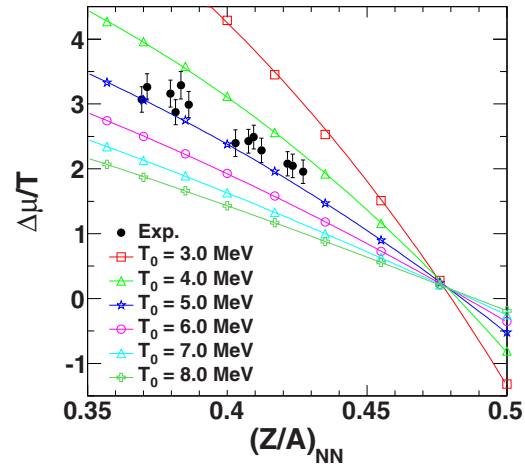

FIG. 7. The comparison between the $\Delta\mu/T$ values from the calculations with different temperature inputs from 3 ∼ 8 MeV and the experimentally extracted primary ones. The curves are the results of polynomial fits to the calculated values for each given T value.

SMM calculations with different initial conditions. As plotted in the figure, $(\Delta\mu/T)_{Pri}$ correlates linearly with $(\Delta\mu/T)_{Sec}$, and this linear relation holds in a wide region of excitation energy and freezeout volume, i.e., $E_x = 5 \sim 10$ MeV and $V/V_0 = 3.0 \sim 10.0$, indicating the breakup process and the statistical decay process are independent of each other. The obtained values of $(\Delta\mu/T)_{Pri}$ and $(\Delta\mu/T)_{Sec}$ under different conditions are globally fit by a linear function and the fitting result is given by

$$(\Delta\mu/T)_{Pri} = 1.25(\Delta\mu/T)_{Sec} + 1.12, \quad (9)$$

where the fitting parameters, 1.25 and 1.12, are only related to the statistical decay process. In order to verify the SMM results, AMD+GEMINI simulations are analyzed for some of reaction systems. The results of the AMD+GEMINI simulations are shown by open circles in the figure and as seen in the figure they are consistent to those of SMM. The scaling relation in Eq. (9) can be applied to the experimental yields to evaluate the sequential effect on the experimentally extracted $\Delta\mu/T$ values quantitatively. The scaling invariance shown in Fig. 6 also suggests that Eq. (9) can be applied to reactions over a wide incident energy region. Using Eq. (9), for all 13 systems, the "primary" $\Delta\mu/T$ values are derived from those of the experimentally observed IMF yields and shown by full circles in Fig. 5 together with the experimentally extracted ones (open circles). The "primary" $\Delta\mu/T$ as a function of $(Z/A)_{NN}$ also shows a monotonic decreasing trend, due to the linear mapping. Since $(Z/A)_{NN}$ is same before and after the sequential decays, the monotonic behavior of the primary $\Delta\mu/T$ as function of $(Z/A)_{NN}$ originates from the characteristic properties of the NN source. This is further utilized to determine the temperature of the NN source and the symmetry energy in the following analysis.

E. Temperature

In order to evaluate the temperature at the time of the fragment formation from the primary $\Delta\mu/T$ values evaluated above, QSM is employed. QSM assumes thermal and chemical equilibrium and the primary fragment formation is characterized by the neutron and proton chemical potentials, which are optimized using quantum statistical distributions at a given density ρ, temperature T and N/Z ratio of the system. It has been applied to study the characteristic nature of the IMF emitting source produced in heavy ion reactions in the energy range of 30 MeV/nucleon to 15 GeV/nucleon [69–73].

As presented in Refs. [69–73], the density and temperature of the source are closely correlated for a given entropy, that is, the temperature increases as the density increases to obtain the same entropy. The entropy is closely related to the experimental isotope yield ratios. In other words, within QSM, one cannot determine the density and temperature values uniquely from the experimental isotope yield ratios. In the present analysis, therefore, the source density of $\rho/\rho_0 = 0.56$, which has been determined from the experimentally reconstructed primary hot isotope yields in the reaction system ^{64}Zn + ^{112}Sn in our previous studies [26,50] is adopted. For the given density of $\rho/\rho_0 = 0.56$, the $\Delta\mu/T$ values of the primary fragments are calculated for different temperatures from $T = 3$ to $T = 8$ MeV and compared with the experimentally extracted primary $\Delta\mu/T$ values in Fig. 7. As plotted in the figure, both QSM and experimentally extracted $\Delta\mu/T$ values show rather consistent decreasing trends as $(Z/A)_{NN}$ increases, and the experimental data points distribute between the calculated ones for $T = 4$ and 5 MeV.

In order to extract an optimum temperature value from the experimental results, a least square analysis is performed by calculating $\chi^2(T)$, where $\chi^2(T)$ for a certain input T is given by

$$\chi^2(T) = \sum_i \frac{[(\Delta\mu/T)_{\exp,i} - (\Delta\mu/T)_{QSM,i}(T)]^2}{\sigma^2_{\exp,i}}. \quad (10)$$

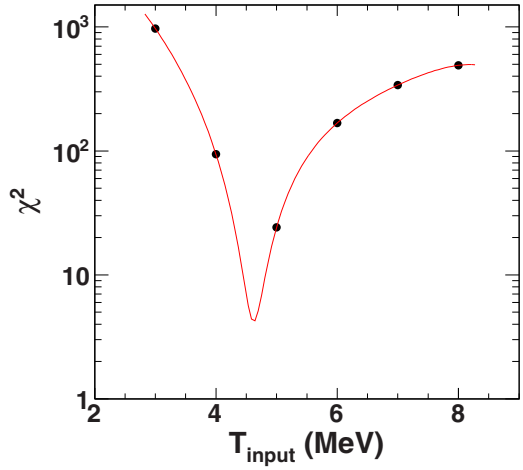

FIG. 8. The resultant $\chi^2(T)$ values as a function of the temperature. The line is the polynomial fit of the data points.

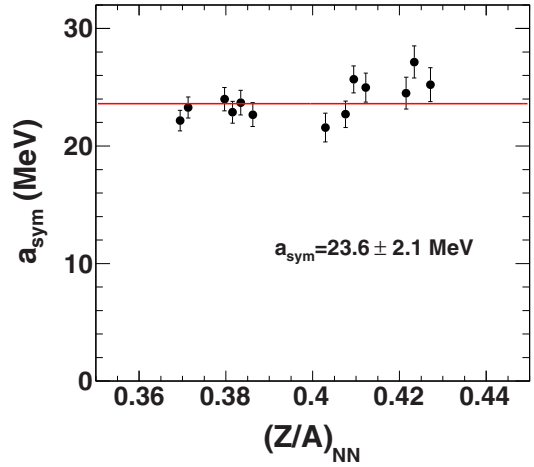

FIG. 9. The resultant $a_{\rm sym}$ values as a function of $(Z/A)_{NN}$ using Eq. (13). The line is the constant fit of the data points.

Here $(\Delta\mu/T)_{{\rm exp},i}$ and $(\Delta\mu/T)_{QSM,i}(T)$ are, respectively, the experimentally extracted and the calculated $\Delta\mu/T$ values for the ith system at a given temperature, and $\sigma_{{\rm exp},i}$ is the corresponding uncertainties. The summation in Eq. (10) is taken over all 13 systems. The resultant $\chi^2(T)$ values are shown in Fig. 8. From this figure, $T = 4.6 \pm 0.4$ MeV is determined and assigned as the temperature at the fragment emission time. The error is from the standard deviation from the fitted experimental curve. This result is consistent with that obtained in our previous work, $T = 5.2 \pm 0.6$ MeV [26], which was extracted from the reconstructed primary hot isotope yields using a self-consistent technique.

F. Density dependent symmetry energy

According to Refs. [1,58], the differential chemical potential is given by

$$\Delta\mu = 2\frac{\partial(E(T,\rho,\delta)/A)}{\partial\delta}. \tag{11}$$

Here, $E(T,\rho,\delta)$ is the total internal energy of the emitting source with N neutrons and Z protons and $\delta = (N-Z)/(N+Z)$. One can calculate the total internal energy using a similar equation to Eq. (6) and therefore the resultant $\Delta\mu$ can be expressed as[1] [74]

$$\Delta\mu = 4\delta a_{\rm sym}(T,\rho) - a_c(\rho)A^{2/3}(1-\delta). \tag{12}$$

From the experiments, $\Delta\mu$ can be calculated as $\Delta\mu = T(\Delta\mu/T)$ from the primary $\Delta\mu/T$ values and the NN-source temperature obtained above. One should note that $a_c(\rho)$ cannot be simply calculated as $a_c(\rho) = T(a_c(\rho)/T)$ from Eq. (8), since the $a_c(\rho)/T$ value there is extracted from the final products after the sequential decays, and does not represent the $a_c(\rho)/T$ value of the primary NN source. Under the assumption of a uniform expansion, the source radius is proportional to $(\rho/\rho_0)^{-1/3}$. Thus $a_c(\rho) = a_c(\rho_0)\cdot(\rho/\rho_0)^{1/3}$, where $a_c(\rho_0) =$ 0.67 MeV [58] is the Coulomb coefficient at the saturation density. In Ref. [26], $a_c(\rho)/T = 0.126$ is extracted from the experimentally reconstructed primary hot fragments at $T = 5.2 \pm 0.6$ MeV, which gives $a_c(\rho) = 0.126(5.2 \pm 0.6) = 0.66 \pm 0.08$ MeV. This value agrees within errors to that used here, that is, $a_c(\rho) = 0.67 \cdot 0.56^{1/3} = 0.55$ MeV. After converting Eq. (12), $a_{\rm sym}$ can be extracted as

$$a_{\rm sym} = \frac{\Delta\mu + a_c(\rho_0)(\rho/\rho_0)^{1/3}A^{2/3}(1-\delta)}{4\delta}. \tag{13}$$

In the $a_{\rm sym}$ extraction, the expected value of the temperature $T = 4.6$ MeV is adopted; $A = A_{NN}$ is calculated using Eq. (1); δ is calculated from $(Z/A)_{NN}$ using Eq. (2). For all 13 available systems, the extracted $a_{\rm sym}$ values are shown as a function of $(Z/A)_{NN}$ in Fig. 9. Their distributions show no clear dependence on $(Z/A)_{NN}$ and $a_{\rm sym} = 23.6 \pm 2.1$ MeV is obtained as an average value. The error is evaluated as the standard deviation from the central value. One should note that this error and the error of the temperature are from the spread of the experimental $\Delta\mu/T$ values around the average ones in both cases and thus the origins are the same. Therefore we take the error of the symmetry energy only from the standard deviation from the average value in Fig. 9.

IV. DISCUSSION

A. Symmetry energy extraction at Fermi energies

In the present analysis, the experimental $\Delta\mu/T$ values extracted from IMF yield ratios, are utilized to extract the temperature and symmetry energy of the fragmenting source in the framework of QSM. The density value of $\rho/\rho_0 = 0.56$ is taken from that in Ref. [26], in which the ^{64}Zn + ^{112}Sn reaction products were analyzed with a self-consistent method in the framework of the AMD model. In both analyses, the experimentally observed isotope yields from the NN-source component are utilized in the MFM formulation. However both analyses are quite different from each other. In the present analysis $\Delta\mu/T$ values, which are directly related to the symmetry energy $a_{\rm sym}$ in Eq. (13), are analyzed.

[1] In Refs. [1,58], Eq. (12) is given without the Coulomb contribution.

They are extracted from the 13 different reaction systems studied at 40 MeV/nucleon, whereas in the self-consistent method five parameters in Eq. (6) were consistently determined using all isotope yields from a single reaction system of ^{64}Zn + ^{112}Sn and the corresponding AMD simulations, using Gogny interactions with three different density-dependent symmetry energy forms [26]. As seen in the formulation of MFM in the Appendix, the density obtained from the IMF yield analysis is closely related to the the density of IMFs when they are formed and therefore closely related to the nuclear matter in a liquid phase. The extracted temperature $T = 4.6 \pm 0.4$ MeV and symmetry energy $a_{\rm sym} = 23.6 \pm 2.1$ MeV in this analysis are common to all 13 reaction systems and consistent with values obtained using the self-consistent method in Ref. [26], i.e., $T = 5.2 \pm 0.6$ MeV and $a_{\rm sym} = 20.8 \pm 0.6$ MeV. As pointed out in Sec. III(a), the NN-source size is around 40 to 90 mass units, as shown in Fig. 2, indicating that the products from the NN source originate from the overlap region of the projectile and target in this energy regime. That is, these particles are produced through a multifragmentation process at a time of freezeout [24]. The extracted common symmetry energy shown in Fig. 9 for all 13 reactions, even though their system size and N/Z value are quite different, is a strong indication that these fragments are produced in a common production mechanism as mentioned earlier.

In Ref. [75], Xu *et al.* studied the temperature and density dependence of symmetry energy and symmetry free energy within a self-consistent thermal model using an isospin and momentum dependent interaction. According to their study, the temperature dependence of these energies at a given density is rather small at $T < 5$ MeV, which suggests that the symmetry energy value of $a_{\rm sym} = 23.6 \pm 2.1$ MeV is close to the symmetry energy value at $T = 0$.

Strictly speaking the symmetry energy in Eq. (6) should be the symmetry free energy according to the derivation in the Appendix where the free energy is used. However as discussed in Ref. [76], the calculated symmetry entropy relative to the temperature value, $S_{\rm sym}/T$, becomes gradually small when the density ρ increases at $\rho = 0.2\rho_0$ toward the normal nuclear density as shown in Fig. 6 of Ref. [76], and at $\rho = 0.56\rho_0$, $S_{\rm sym}/T \sim 0.2$. Therefore the expected difference between the symmetry energy and the symmetry free energy at $T = 4.6$ MeV and $\rho \sim 0.56\rho_0$ is an order of 1 MeV.

It is worth noting a recent work of Brown [77], in which the energy-density functional of nuclear matter was studied using Skyrme interactions, evaluated under the constraints of several experimental values of ground state doubly magic nuclei. According to the extracted narrow bounded energy-density functional, the symmetry energy value of around 24.5 MeV is obtained at $\rho = 0.1$ fm$^{-3} \sim 0.65\rho_0$, which is very close to the values extracted in this analysis. This energy-density point, as pointed out in his work, corresponds to a crossing point in the equation of state that is more or less independent of the neutron skin thickness.

B. Symmetry energy constraint at subsaturation densities

In another previous work [76], the density, temperature and symmetry energy of dilute warm nuclear matter were experimentally extracted in collisions of ^{40}Ar + ^{112}Sn, ^{124}Sn, and ^{64}Zn + ^{112}Sn, ^{124}Sn at 47 MeV/nucleon. In that analysis, yields and energy spectra of early emitted light charged particles from the NN source were analyzed within a coalescence model. The particle multiplicity of the NN source is dominated by these light particles and the extracted density is the density around these light particles. Therefore the extracted density is closely related to the gas phase of the nuclear matter during the collisions in contrast to the results shown in the present analysis. In the coalescence model, the density is closely related to the coalescence radius determined from the yield relationships between the light particles. The extracted density is rather small in the range of $\rho/\rho_0 = 0.03$ to 0.2, indicating that the relative multiplicity of these light particles is governed by the final state interaction between nucleons and clusters in a dilute warm nuclear matter. The temperature values of ~4–11 MeV were determined as a function of the surface velocity of the LCPs, using the H-He double ratio thermometer as a function of the surface velocity of the LCPs. The surface velocity is closely related to the emission time of the LPCs [78]. Symmetry free energy values were extracted from the measured isoscaling parameter values, utilizing the relation $\alpha = a_{\rm sym}/T \cdot [\Delta(Z/A)^2]$. Using the extracted parameters at a given surface velocity, combined with the quantum statistical (QS) approach of Röpke *et al.* [79–82], symmetry energy values were extracted. The corresponding symmetry energy values vary from ~7 MeV to ~11 MeV at the density range of $\rho/\rho_0 = 0.03$ to 0.2.

In Fig. 10, the density dependent symmetry energy obtained in the above two experiments and other experimentally extracted results from various observables are summarized. Details about the cited experimental results are given in Table I. All of data points cited are all the results which are determined based on the nuclear reactions [26,32,59,76,83–88], whereas the shaded area is that from the fit of the properties of the nuclei on the ground and low-excited states [89].

In Fig. 10, two groups are clearly identified, which are at $0.1 \lesssim \rho/\rho_0 \leqslant 1.0$ and $\rho/\rho_0 \lesssim 0.1$, respectively. At $0.1 \lesssim \rho/\rho_0 \leqslant 1.0$, the existing data points are consistent with each other within the errors and distribute along a line as a function of ρ/ρ_0. This fact is in good agreement with the prediction of the mean-field theory. Following the mean-field theory, the density dependent symmetry energy is phenomenologically parameterized as a power function,

$$a_{\rm sym}(\rho/\rho_0) = a_{\rm sym}^{\rho=\rho_0}(\rho/\rho_0)^{\gamma}, \tag{14}$$

where $a_{\rm sym}^{\rho=\rho_0}$ is the symmetry energy value at the saturation density, and γ is a parameter for describing the "stiffness" of the density dependent symmetry energy. This symmetry energy formulation has been adopted in many statistical and transport models. As "free" parameters, $a_{\rm sym}^{\rho=\rho_0}$ and γ can be extracted by performing the global fit of the existing data points at $0.1 \lesssim \rho/\rho_0 \leqslant 1.0$ using Eq. (14). This fitting result is shown by a blue line in Fig. 10 and given by

$$a_{\rm sym}(\rho/\rho_0) = 31.6(\rho/\rho_0)^{0.69}. \tag{15}$$

At the saturation density, the slope parameter can be also calculated by the relation of $L = 3\gamma a_{\rm sym}^{\rho=\rho_0}$ as $L = 65.4$ MeV.

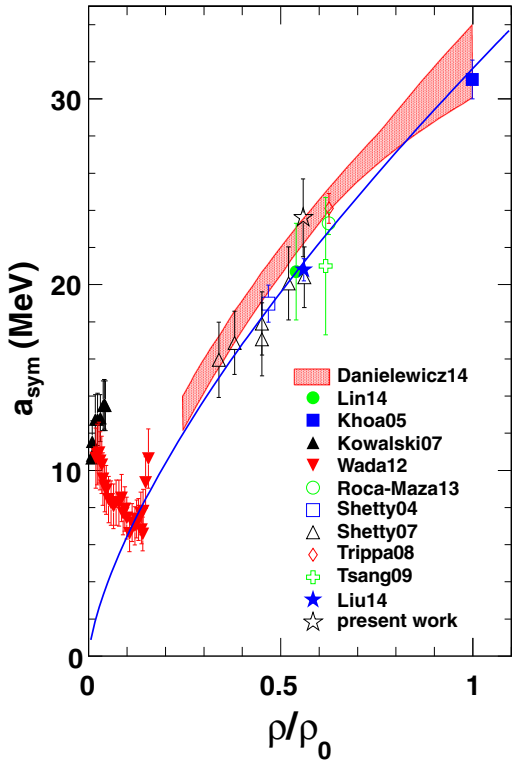

FIG. 10. Summary of the density dependent symmetry energy obtained in the present and previous studies. The line is the fit of the existing data points at $0.1 \leqslant \rho/\rho_0 \leqslant 1.0$ using Eq. (14).

This constraint using the reaction-related observables is compared with that proposed by Danielewicz *et al.* in Ref. [89] (shaded area), where a combination constraint of isobaric analog states and neutron-proton skins was performed. In their analysis, the symmetry energy coefficient was expressed as the sum of the volume and surface contributions and their values were evaluated separately. For the net symmetry energy, they set a constraint for $a_{\rm sym}$ and γ at the saturation density in $a_{\rm sym}^{\rho=\rho_0} = 30.2 \sim 33.7$ MeV and $\gamma = 0.36 \sim 0.74$, respectively, and the slope parameter was constrained as $L = 35 \sim 70$ MeV. Both the constraints of our present work and of Danielewicz *et al.* suggest a stiff, but softer than linear, form of symmetry energy at subsaturation densities.

TABLE I. Summary on the cited data from various independent studies.

Ref.	Year	Experimental measurement
Danielewicz *et al.* [89]	2014	Isobaric analog states, ΔR_{np}
Lin *et al.* [59]	2014	Reconstructed isotopic yield
Khoa *et al.* [83]	2005	Elastic scattering, charge exchange
Kowalski *et al.* [84]	2007	LCP production
Wada *et al.* [76]	2012	LCP production
Roca-Maza *et al.* [85]	2013	Giant quadrupole resonance
Shetty *et al.* [86]	2004	Isoscaling
Shetty *et al.* [87]	2007	Isoscaling
Trippa *et al.* [32]	2008	Giant dipole resonance
Tsang *et al.* [88]	2009	Isospin diffusion, neutron-proton ratio
Liu *et al.* [26]	2015	Reconstructed isotopic yield

At lower densities ($\rho/\rho_0 \lesssim 0.1$), the experimentally extracted symmetry energy values significantly deviate from the mean-field prediction as shown in Fig. 10. This significant deviation has been attributed to the formation of clusters at low densities, well described by the QS approach which includes cluster correlations in the medium [76,90,91]. Further investigations are urgently required for a better understanding of the clusterization mechanism in low density matter, due to its critical applications in both nuclear and astrophysical physics [91].

V. SUMMARY

Within the framework of MFM, values of $\Delta\mu/T$, the ratios of neutron-proton differential chemical potential values to the temperature, are experimentally extracted from isotope yields of 13 reaction systems at 40 MeV/nucleon. After evaluation of the secondary decay effect on $\Delta\mu/T$ with the help of SMM, the resultant primary $\Delta\mu/T$ values are compared to those from QSM simulations to determine the temperature and symmetry energy values of the fragmenting system. Using the density value of $\rho/\rho_0 = 0.56$ from a previous analysis [26], the temperature and symmetry energy values of $T = 4.6 \pm 0.4$ MeV and $a_{\rm sym} = 23.6 \pm 2.1$ MeV are extracted. These values agree well with those of the previous work in Ref. [26], in which a different method was utilized. Following the mean-field theory, the density dependent symmetry energies at $0.1 \lesssim \rho/\rho_0 \leqslant 1.0$ are phenomenologically parametrized as a power function, $a_{\rm sym}(\rho/\rho_0) = 31.6(\rho/\rho_0)^{0.69}$, by performing a global fit to the symmetry energy values obtained in the present work and those experimentally extracted from other studies. At lower densities ($\rho/\rho_0 \lesssim 0.1$), the experimentally extracted symmetry energy values significantly deviate from the mean-field prediction, and this fact is attributed to the clusterization mechanism in a dilute warm nuclear matter.

ACKNOWLEDGMENTS

We thank the staff of the Texas A&M Cyclotron facility for their support during the experiment. We thank the Institute of Nuclear Physics of the University of Louvain and Prof. Y. ElMasri for allowing us to use the DEMON detectors. We thank W. Trautmann for providing the QSM code used in this study. We also thank A. Ono and R. J. Charity for their AMD and GEMINI codes available to us. R.W. thanks the program of the Visiting Professorship of Senior International Scientists of the Chinese Academy of Science for the supports. This work was supported by the CAS program of Light of West China Program under Grant No. Y601030XB0, the National Basic Research Program of China (973 Program) under Grant No. 2014CB845405, and the National Natural Science Foundation of China under Grant No. 11205209. This work was also supported by the US Department of Energy under Grant No. DE–FG03–93ER40773 .

APPENDIX: MODIFIED FISHER MODEL (MFM)

Free energy is formulized as two types,

$$F = U - TS, \tag{A1}$$

$$F = H - TS. \tag{A2}$$

Equation (A1) is the Helmholtz free energy which is obtain from a process under the condition of a constant volume, whereas Eq. (A2) is the Gibbs free energy from a process under the condition of a constant pressure.

In the Fisher model [42], for a single constituent system, a spherical droplet from A particles is formed in the gas phase with B particles through a phase transition and both phases are derived from a parent source with mass $A + B$ particles. The free energy of the system in the initial and final phases can be written, respectively, as

$$F_{\text{initial}} = \mu_g(A + B) - TS, \tag{A3}$$

$$F_{\text{final}} = \mu_l A + \mu_g B + 4\pi R^2\sigma - T(S - \tau \ln A). \tag{A4}$$

In Eqs. (A3) and (A4), μ_l and μ_g are, respectively, the chemical potentials of liquid and gas phases, and S is the total entropy of the initial phases. τ is the critical exponent and T is the system temperature. The third term in Eq. (A4) is the surface contribution for the spherical droplet with radius $R\,(R = r_0 A^{1/3})$ and surface tension parameter σ. σ near the critical point can be expressed as a function of temperature as

$$\sigma(T, T_c) = \begin{cases} \sigma_0\left(1 + \frac{3T}{2T_c}\right)\left(1 - \frac{T}{T_c}\right)^{3/2} & (T < T_c) \\ 0 & (T \geqslant T_c), \end{cases} \tag{A5}$$

where T_c is the temperature at the critical point. The last term in Eq. (A4) originates from the entropy change of the system when the droplet is formed. The term $\tau \ln A$ is the entropy change caused by the droplet, introduced by Fisher in his model [42]. The free energy of the droplet can be given as the difference between Eqs. (A3) and (A4) as

$$\begin{aligned} F_{\text{droplet}} &= F_{\text{final}} - F_{\text{initial}} \\ &= (\mu_l - \mu_g)A + 4\pi r_0^2 \sigma A^{2/3} + T\tau \ln A. \end{aligned} \tag{A6}$$

In a canonical ensemble, free energy can be deduced as

$$-F_{\text{droplet}} = T \ln(\mathbf{Z}), \tag{A7}$$

where $\mathbf{Z}$ is the partition function and it is proportional to the yield $Y(A)$ of a given type of droplets with A particles,

$$Y(A) \propto \mathbf{Z} = \exp\left(-\frac{F_{\text{droplet}}}{T}\right). \tag{A8}$$

Equation (A8) is the mathematical expression of Fisher model.

In order to apply the Fisher model to a nuclear multifragmentation process, two constituents (neutrons and protons) and the characteristics of nuclear force have to be taken into account in the model. In the framework of MFM, from the analogy to Eq. (A6), the free energy of a fragment with mass number A and $I = N - Z$ (N neutrons and Z protons) is expressed as

$$\begin{aligned} F(I, A) = (&-W(I, A) - \mu_n N - \mu_p Z) \\ &+ T(\tau \ln A - S_{\text{mix}}(N, Z)). \end{aligned} \tag{A9}$$

Following Ref. [44], utilizing the generalized Weizsäcker-Bethe semiclassical mass formula [4,5], $W(I, A)$ is given as Eq. (6) in the text. $S_{\text{mix}}(N, Z)$ is called mixing entropy, which originates from the change from a single constituent system to a two constituent system. For classical particles, the total number of the microstates, $\Omega_{M.B.}$ can be expressed as

$$\Omega_{M.B.} = \frac{N_0!}{\Pi a_l!} \Pi \omega_l^{a_l}!, \tag{A10}$$

where N_0 is the particle number and a_l is the particle number at the l state, that $N_0 = \Sigma a_l$. ω_l is the degeneracy of the l state. Going to a nuclear system, ignoring the spin, nucleons only have two "states", proton and neutron, defining as "n" state and "p" state here. The degeneracies of two states are both 1. Therefore for a nuclei with Z protons ($a_p = Z$) and N neutrons ($a_n = N$), the total number of the microstates becomes

$$\Omega_{M.B.}(N, Z) = \frac{A!}{N!Z!}. \tag{A11}$$

Thus $S_{\text{mix}}(N, Z)$ is simply calculated as

$$\begin{aligned} S_{\text{mix}}(N, Z) &= \ln(A!) - \ln(N!Z!) \\ &= \left[A(\ln A - 1) + \frac{1}{2}\ln(2\pi A)\right] - \left[N(\ln N - 1) + \frac{1}{2}\ln(2\pi N) + Z(\ln Z - 1) + \frac{1}{2}\ln(2\pi Z)\right] \\ &\approx A(\ln A - 1) - [N(\ln N - 1) + Z(\ln Z - 1)] \\ &= -\left[N \ln\left(\frac{N}{A}\right) + Z \ln\left(\frac{Z}{A}\right)\right]. \end{aligned} \tag{A12}$$

Combining Eqs. (6), (A9), and (A12), one can get

$$F(I, A) = \left(-\widetilde{a_v} - \frac{\delta}{2}\Delta\mu\right)A + a_s A^{2/3} + T\left[\tau \ln A + N \ln\left(\frac{N}{A}\right) + Z \ln\left(\frac{Z}{A}\right)\right] + a_c \frac{Z(Z-1)}{A^{1/3}} + a_{\text{sym}} \frac{(N-Z)^2}{A} + a_p \frac{\delta_p}{A^{1/2}}, \tag{A13}$$

where $\widetilde{a_v} = a_v + \frac{1}{2}(\mu_n + \mu_p)$, $\Delta\mu = \mu_n - \mu_p$, and $\delta = (N - Z)/A$. Comparing Eqs. (A6) and (A13), we can see the correspondence between a liquid-gas transition and a nuclear multifragmentation process as

$$\begin{aligned}(\mu_l - \mu_g)A &\Longleftrightarrow \left(-\widetilde{a_v} - \frac{\delta}{2}\Delta\mu\right)A,\\ 4\pi r_0^2 \sigma A^{2/3} &\Longleftrightarrow a_s A^{2/3}\\ T\tau \ln A &\Longleftrightarrow T\left[\tau \ln A + N \ln\left(\frac{N}{A}\right) + Z \ln\left(\frac{Z}{A}\right)\right].\end{aligned} \tag{A14}$$

Other terms, such as Coulomb, symmetry, and pairing terms, are added in Eq. (A13) for the nuclear matter application.

[1] B. A. Li, L. W. Chen, and C. M. Ko, Phys. Rep. **464**, 113 (2008).
[2] J. M. Lattimer and M. Prakash, Phys. Rep. **442**, 109 (2007).
[3] M. R. D. Rodrigues *et al.*, Phys. Rev. C **88**, 034605 (2013).
[4] C. F. von Weizsäcker, Z. Phys. **96**, 431 (1935).
[5] H. A. Bethe, Rev. Mod. Phys. **8**, 82 (1936).
[6] D. H. E. Gross, Rep. Prog. Phys. **53**, 605 (1990).
[7] J. Bondorf, A. S. Botvina, A. S. Iljinov, I. N. Mishutin, and K. Sneppen, Phys. Rep. **257**, 133 (1995).
[8] J. Aichelin and G. Bertsch, Phys. Rev. C **31**, 1730 (1985).
[9] H. Kruse, B. V. Jacak, J. J. Molitoris, G. D. Westfall, and H. Stöcker, Phys. Rev. C **31**, 1770 (1985).
[10] V. Baran *et al.*, Nucl. Phys. A **703**, 603 (2002).
[11] J. Aichelin, Phys. Rep. **202**, 233 (1991).
[12] M. Papa, G. Giuliani, and A. Bonasera, J. Comput. Phys. **208**, 403 (2005).
[13] N. Wang, Z. Li, and X. Wu, Phys. Rev. C **65**, 064608 (2002).
[14] A. Ono and H. Horiuchi, Prog. Part. Nucl. Phys. **53**, 501 (2004).
[15] H. Feldmeier, Nucl. Phys. A **515**, 147 (1990).
[16] S. Piantelli *et al.*, Nucl. Phys. A **809**, 111 (2008).
[17] K. Zbiri *et al.*, Phys. Rev. C **75**, 034612 (2007).
[18] A. Ono, H. Horiuchi, and T. Maruyama, Phys. Rev. C **48**, 2946 (1993).
[19] A. Ono and H. Horiuchi, Phys. Rev. C **53**, 2958 (1996).
[20] A. Ono, Phys. Rev. C **59**, 853 (1999).
[21] A. Ono, S. Hudan, A. Chbihi, and J. D. Frankland, Phys. Rev. C **66**, 014603 (2002).
[22] R. Wada *et al.*, Phys. Rev. C **62**, 034601 (2000).
[23] R. Wada *et al.*, Phys. Rev. C **69**, 044610 (2004).
[24] X. Liu *et al.*, Phys. Rev. C **92**, 014623 (2015).
[25] X. Liu *et al.*, Phys. Rev. C **90**, 014605 (2014).
[26] X. Liu *et al.*, Nucl. Phys. A **933**, 290 (2015); X. Liu *et al.*, Nucl. Phys. A (to be published).
[27] M. B. Tsang, W. A. Friedman, C. K. Gelbke, W. G. Lynch, G. Verde, and H. S. Xu, Phys. Rev. Lett. **86**, 5023 (2001).
[28] M. B. Tsang *et al.*, Phys. Rev. Lett. **92**, 062701 (2004).
[29] M. A. Famiano *et al.*, Phys. Rev. Lett. **97**, 052701 (2006).
[30] T. Li *et al.*, Phys. Rev. Lett. **99**, 162503 (2007).
[31] A. Klimkiewicz *et al.*, Phys. Rev. C **76**, 051603(R) (2007).
[32] L. Trippa, G. Colò, and E. Vigezzi, Phys. Rev. C **77**, 061304(R) (2008).
[33] Z. Kohley *et al.*, Phys. Rev. C **85**, 064605 (2012).
[34] H. S. Xu *et al.*, Phys. Rev. Lett. **85**, 716 (2000).
[35] M. B. Tsang *et al.*, Phys. Rev. C **64**, 054615 (2001).
[36] A. Ono, P. Danielewicz, W. A. Friedman, W. G. Lynch, and M. B. Tsang, Phys. Rev. C **68**, 051601(R) (2003).
[37] A. Ono, P. Danielewicz, W. A. Friedman, W. G. Lynch, and M. B. Tsang, Phys. Rev. C **70**, 041604(R) (2004).
[38] Z. Chen *et al.*, Phys. Rev. C **81**, 064613 (2010).
[39] M. Huang *et al.*, Phys. Rev. C **81**, 044620 (2010).
[40] M. Huang *et al.*, Phys. Rev. C **82**, 054602 (2010).
[41] M. Huang *et al.*, Nucl. Phys. A **847**, 233 (2010).
[42] M. E. Fisher, Rep. Prog. Phys. **30**, 615 (1967).
[43] R. W. Minich *et al.*, Phys. Lett. B **118**, 458 (1982).
[44] A. S. Hirsch *et al.*, Nucl. Phys. A **418**, 267 (1984).
[45] A. Bonasera *et al.*, Phys. Rev. Lett. **101**, 122702 (2008).
[46] D. Hahn and H. Stöcker, Nucl. Phys. A **476**, 718 (1988).
[47] F. Hubert, R. Bimbot, and H. Gauvin, At. Data Nucl. Data Tables **46**, 1 (1990).
[48] I. Tilquin *et al.*, Nucl. Instrum. Methods Phys. Res. A **365**, 446 (1995).
[49] S. Zhang *et al.*, Nucl. Instrum. Methods Phys. Res. A **709**, 68 (2013).
[50] W. Lin *et al.*, Phys. Rev. C **90**, 044603 (2014).
[51] R. Wada *et al.*, Phys. Rev. C **39**, 497 (1989).
[52] See Supplemental Material at http://link.aps.org/supplemental/10.1103/PhysRevC.95.044601 for the extracted multiplicity values of the NN source of neutrons, LCPs, and IMFs for all available 13 reactions.
[53] R. Lionti *et al.*, Phys. Lett. B **625**, 33 (2005).
[54] J. Rizzo *et al.*, Nucl. Phys. A **806**, 79 (2008).
[55] A. Bonasera *et al.*, Riv. Nuovo Cimento **23**, 1 (2000).
[56] L. G. Sobotka, Phys. Rev. C **84**, 017601 (2011).
[57] P. Marini *et al.*, Phys. Rev. C **85**, 034617 (2012).
[58] P. Danielewicz and J. Lee, Nucl. Phys. A **818**, 36 (2009).
[59] W. Lin *et al.*, Phys. Rev. C **89**, 021601(R) (2014); **95**, 039907(E) (2017).
[60] T. X. Liu *et al.*, Phys. Rev. C **69**, 014603 (2004).
[61] R. J. Charity *et al.*, Nucl. Phys. A **483**, 371 (1988).
[62] J. P. Bondorf, R. Donangelo, and I. N. Mishustin, Nucl. Phys. A **443**, 321 (1985).
[63] S. Das Gupta and A. Z. Mekjian, Phys. Rev. C **57**, 1361 (1998).
[64] K. A. Bugaev, M. I. Gorenstein, I. N. Mishustin, and W. Greiner, Phys. Lett. B **498**, 144 (2001).
[65] G. Chaudhuri and S. Das Gupta, Phys. Rev. C **80**, 044609 (2009).
[66] A. S. Botvina *et al.*, Nucl. Phys. A **584**, 737 (1995).
[67] C. Williams *et al.*, Phys. Rev. C **55**, R2132 (1997).
[68] R. P. Scharenberg *et al.*, Phys. Rev. C **64**, 054602 (2001).
[69] A. S. Botvina, O. V. Lozhkin, and W. Trautmann, Phys. Rev. C **65**, 044610 (2002).
[70] W. Trautmann *et al.*, Phys. Rev. C **76**, 064606 (2007).
[71] R. Wada *et al.*, Phys. Rev. Lett. **58**, 1829 (1987).

[72] R. Trockel *et al.*, Phys. Rev. C **38**, 576 (1988).
[73] O. V. Lozhkin and W. Trautmann, Phys. Rev. C **46**, 1996 (1992).
[74] H. A. Bethe *et al.*, Aston. Astrophys. **7**, 279 (1970).
[75] J. Xu, L.-W. Chen, B.-A. Li, and H.-R. Ma, Phys. Rev. C **75**, 014607 (2007).
[76] R. Wada *et al.*, Phys. Rev. C **85**, 064618 (2012).
[77] B. A. Brown, Phys. Rev. Lett. **111**, 232502 (2013).
[78] J. Wang *et al.*, Phys. Rev. C **72**, 024603 (2005).
[79] C. Kuhrts, M. Beyer, P. Danielewicz, and G. Röpke, Phys. Rev. C **63**, 034605 (2001).
[80] G. Röpke, Phys. Rev. C **79**, 014002 (2009).
[81] S. Typel, G. Röpke, T. Klähn, D. Blaschke, and H. H. Wolter, Phys. Rev. C **81**, 015803 (2010).
[82] G. Röpke, Nucl. Phys. A **867**, 66 (2011).
[83] D. T. Khoa and H. S. Than, Phys. Rev. C **71**, 044601 (2005).
[84] S. Kowalski *et al.*, Phys. Rev. C **75**, 014601 (2007).
[85] X. Roca-Maza *et al.*, Phys. Rev. C **87**, 034301 (2013).
[86] D. V. Shetty *et al.*, Phys. Rev. C **70**, 011601(R) (2004).
[87] D. V. Shetty, S. J. Yennello, and G. A. Souliotis, Phys. Rev. C **76**, 024606 (2007).
[88] M. B. Tsang, Y. Zhang, P. Danielewicz, M. Famiano, Z. Li, W. G. Lynch, and A. W. Steiner, Phys. Rev. Lett. **102**, 122701 (2009).
[89] P. Danielewicz and J. Lee, Nucl. Phys. A **922**, 1 (2014).
[90] J. B. Natowitz *et al.*, Phys. Rev. Lett. **104**, 202501 (2010).
[91] K. Hagel *et al.*, Eur. Phys. J. A **50**, 39 (2014).